ROYAL SOCIETY
OF CHEMISTRY

PAPER

Check for updates

Layered tellurides: stacking faults induce low thermal conductivity in the new In$_2$Ge$_2$Te$_6$ and thermoelectric properties of related compounds†

Robin Lefèvre, [ID] [a] David Berthebaud,[a] Oleg Lebedev,[a] Olivier Pérez,[a] Célia Castro,[b] Stéphanie Gascoin,[a] Daniel Chateigner [ID] [a] and Franck Gascoin [ID] *[a]

A new ternary layered compound In$_2$Ge$_2$Te$_6$, belonging to the hexatellurogermanate family has been synthesized from the reaction of appropriate amounts of the pure elements at high temperature in sealed silica tubes. In$_2$Ge$_2$Te$_6$ crystallizes in the rhombohedral space-group $R\bar{3}$:H with lattice parameters $a = 7.0863(3)$ Å and $c = 21.206(2)$ Å and its structure is resolved using single crystal X-ray diffraction. The transport properties (Seebeck coefficient, resistivity and thermal conductivity) of compounds belonging to the family AMTe$_3$ (A = In and Cr; M = Ge and Si) are reported. All compounds are p-type semiconductors. InSiTe$_3$ and Cr$_2$Si$_2$Te$_6$ are too resistive to be good thermoelectric materials, with maximal power factors of 10^{-6} and 10^{-5} W m^{-2} K^{-2} at 473 K, while In$_2$Ge$_2$Te$_6$ and Cr$_2$Ge$_2$Te$_6$ exhibit maximal values of about 10^{-4} and 10^{-3} W m^{-2} K^{-2} at 673 K, respectively. All compounds exhibit thermal conductivity below 2 W m^{-1} K^{-1}, with values dropping to 0.35 W m^{-1} K^{-1} at 673 K for In$_2$Ge$_2$Te$_6$. Transmission electron microscopy evidences stacking faults explaining such low thermal conductivities. The best ZT values are observed for Cr$_2$Ge$_2$Te$_6$ with 0.45 at 773 K and In$_2$Ge$_2$Te$_6$ with 0.18 at 673 K. Among these layered structures, a spark plasma sintered Cr$_2$Ge$_2$Te$_6$ sample exhibits some thermal conductivity anisotropy but only weakly due to crystallite orientations.

1. Introduction

Transition metal chalcogenides exhibit various remarkable properties making them of primary importance. This interest has been even further increased by the discovery of superconductivity in the mixed valence system A$_x$Fe$_{2-y}$Se$_2$ (ref. 1) and by the promising thermoelectric properties of several systems like A$_x$TiCh$_2$, with Ch = S or Se (ref. 2–4) or the tetrahedrites of the general formula Cu$_{12}$Sb$_4$S$_{13}$.[5,6] Furthermore, we have recently demonstrated that complex polar transition metal chalcogenides often offer structural features leading to extremely low lattice thermal conductivity.[7–12] Indeed, structures containing infinite 1D-channels (like pseudo-hollandites) or layered structures (TiCh$_2$ of CdI$_2$ type or the title compounds) have the propensity to accommodate structural point defects such as mixed or partial occupancy, or extended defects such as stacking defaults, dislocation, or slip planes. Subsequently, one consequence of these defects is the extremely low lattice thermal conductivity, well below 1 W m^{-1} K^{-1}, a primordial prerequisite for, *in fine*, obtaining interesting thermoelectric properties.

Within layered compounds, those adopting the general formula AMCh$_3$ are numerous as they can be made from a large number of combinations of various A, M and Ch with A = In,[13] Cr,[14–17] V,[17] Mn,[18,19] Al[20] or Fe;[21,22] M = Si, Ge or P, and Ch = S, Se or Te. Even though this crystal structure is well known, only a few systems have had their transport properties characterized.[16,19,23] Interestingly, the thermoelectric properties of Cr$_2$Ge$_2$Te$_6$ were reported during our own investigation in these systems.[24] Here we report the discovery of a new compound In$_2$Ge$_2$Te$_6$ and the properties of four compounds AMTe$_3$ with A = In or Cr, and M = Si or Ge. In this contribution, we also discuss the reason behind the extremely low thermal conductivity of these compounds and study by quantitative texture analysis the possible anisotropy of the transport properties of dense polycrystalline samples.

2. Experimental details

For safety reasons and in order to prevent the oxidation of the reactants and products, all manipulations were performed under inert gas or vacuum (glovebox or sealed containers). The elements, Cr (powder -325 mesh, 99%), Ge (powder -100 mesh, 99.999%), In (tear drops 4 mm, 99.9%), Si (powder -100 mesh, 99.9%) and Te (lumps, 99.999+%), all from Alfa Aesar, were used as received.

[a]Normandie Univ, ENSICAEN, UNICAEN, CNRS, IUT-Caen, CRISMAT, 14000 Caen, France. E-mail: franck.gascoin@ensicaen.fr; Tel: +33 2 31 45 26 05

[b]Normandie Univ, UNIROUEN, INSA Rouen, CNRS, GPM, 76000 Rouen, France

† Electronic supplementary information (ESI) available. See DOI: 10.1039/c7ta04810f

2.1. Single crystal synthesis and structure refinement

The single crystals used for structural determination have been grown from a 0.7 g stoichiometric mixture of In, Ge and Te placed in a sealed (under vacuum) fused silica tube. The mixture was heated in 6 hours up to 723 K, the temperature at which it remained for 5 days, and then cooled down to room temperature within 6 hours. Black shiny platelet-like crystals were manually selected for structural investigation.

Single-crystal X-ray diffraction analyses were performed using Mo $K\alpha_1$ radiation produced with a Microfocus Incoatec IµS sealed X-ray tube on a KappaCCD (Bruker-Nonius) four circles diffractometer equipped with a 2D CCD detector. The data collection consists of large Ω and φ scans of the reciprocal space. The frames were integrated with the Bruker SAINT software package[25] using a narrow-frame algorithm in APEX2.[26] The final cell parameters are based on the refinement of the XYZ-centroids of more than a thousand reflections above 20 $\sigma(I)$ with 2θ larger than 75°. The data were corrected for absorption using the Sadabs program,[27] developed for scaling and absorption corrections of area detector data. The space group determination, structural determination and refinement were performed using charge flipping with the Superflip algorithm[28] within Jana2006.[29]

2.2. Powder synthesis and sintering process

All powder syntheses have been performed using stoichiometric amounts of the elements in order to obtain 7 to 8 g of the desired compound. To minimize the amount of impurities due to the phase incongruent melting, various synthesis methods and temperature cycles have been used depending on the compounds.

To synthesize $InSiTe_3$ and $Cr_2Si_2Te_6$, the temperature was raised to 773 K in 7 hours and maintained for 10 hours and further raised to 1123 K in 7 hours and maintained for a day. The mixture was cooled down to room temperature in a day.

In order to obtain a homogeneous fine and reactive powder of nominal Cr:2;Ge:2;Te:6 and In:2;Ge:2;Te:6, we first ground all the elements using mechanical alloying using appropriate amounts of the elements loaded in 20 ml tungsten carbide jars and using 7 balls of the same material. The mechanical grinding was achieved using a Fritsch Pulverisette 7 PL, for 8 cycles of 15 minutes at a speed of 600 rpm. The ground mixture was then pressed into a pellet and loaded into a sealed silica tube under vacuum. The pellets were annealed at 673 K for two days.

Powders were then compacted using spark plasma sintering (SPS FCT HP D 25/1) in order to produce dense samples for physical property measurements. About 5 to 6 g of samples were inserted into a high density graphite die (Carbone Lorraine) with an inner diameter of 15 mm for $Cr_2Si_2Te_6$ and $InSiTe_3$ or 10 mm for $Cr_2Ge_2Te_6$ and $In_2Ge_2Te_6$ using various conditions (STable 1†). The bulk densities of each sample were determined by Archimedes' method using ethanol as the displacement medium and were found to be over 95% of the theoretical densities. The samples were stored in air and checked multiple times using X-ray powder diffraction measurements, which showed no sign of degradation or oxidation after several weeks.

2.3. Powder and textured sample characterization

The quality of the samples was checked at each step of the process by means of X-ray powder diffraction using an X-Pert Pro Panalytical diffractometer working with Cu $K_{\alpha1}/K_{\alpha2}$ radiation ($\lambda_1 = 1.540598$ Å and $\lambda_2 = 1.544426$ Å) and equipped with a PIXEL detector. Le Bail fitting and Rietveld refinement have been performed using the FullProf software[30] included in WinPLOTR.[31]

The $In_2Ge_2Te_6$ sample was ground under ethanol, and the resulting dispersion was transferred to a holey carbon film fixed on a 3 mm copper grid. Electron diffraction and high-angle annular dark field (HAADF)-scanning TEM (STEM) studies were performed using a JEM ARM 200F cold FEG double aberration corrected electron microscope operated at 200 kV and equipped with a large solid-angle CENTURIO EDX detector.

After SPS sintering, the transport properties of the $Cr_2Ge_2Te_6$ polycrystalline sample exhibit some anisotropy (see Section 3.4). Quantitative texture characterization was thus performed within the combined analysis formalism[32] implemented in the MAUD software.[33] This methodology, based on a cyclic Rietveld refinement of a series of X-ray diagrams measured at different sample orientations, enables quantitative determination of sample features like texture, structure, residual stresses, crystallite sizes, shapes and microdistortions, phase contents, etc. An X-ray four-circle diffractometer setup equipped with a curved position sensitive detector (CPS120 from Thermo Scientific, France), using monochromatized CuKα average radiation was used.[34] Due to the relatively low expected texture strength in such samples, 2θ diagrams using a regular 5° × 5° grid in tilt and azimuth angles (χ and Φ, respectively) with $0° \leq \chi \leq 55°$ and $0° \leq \Phi \leq 355°$ were measured. It resulted in 792 diagrams, each one exhibiting nearly 4000 measured points. We used an incident angle of the X-ray beam on the sample plane of $\omega = 20°$, centered on the main Bragg peaks range for the phase of concern. The crystallite orientation distribution (OD) and normalized pole figures calculated from it were refined using the E-WIMV algorithm[35] after extraction of the peak intensities during the Rietveld cycles. OD and refinement reliabilities are estimated using conventional reliability factors.[36] More details concerning texture and combined analysis would be beyond the scope of this work and are advantageously found elsewhere.[33] We used the initial structure definition of $Cr_2Ge_2Te_6$ ($R\bar{3}$:H space group) given in the Crystallography Open Database no. 1543733.[16] The sample reference frame is given by the direction of the axial pressure applied during the SPS sintering (P_{SPS}), or $\parallel$ direction, which corresponds to the centers of the pole figures (Z). We could not detect any residual strains within our experimental resolution, that is, the residual stresses, if existing, are estimated to be lower than 10 MPa. Crystallite sizes, shapes, and microstrains were refined using the Popa description.[37] We estimate that our X-ray combined analysis setup probed several millions of crystallites. The instrumental contribution was calibrated using the 660b LaB_6 powder standard from NIST.

2.4. Transport properties

High temperature measurements were performed from room temperature to a maximum of 473 K ($InSiTe_3$ and $Cr_2Si_2Te_6$), 673 K ($In_2Ge_2Te_6$) and 773 K ($Cr_2Ge_2Te_6$). The high temperature resistivity (ρ) and Seebeck coefficient (S) were measured with a ZEM-3 system (Ulvac) by using the four-probe method and differential method, respectively, on approximately $2.5 \times 2.5 \times 10$ mm^3 bars. The measurements (taken both upon heating and cooling of the samples) were performed under helium partial pressure. The high temperature thermal diffusivity was measured by the laser flash method using a LFA-457 apparatus (Netzsch) on square samples of $6 \times 6 \times 0.7$ mm^3. The specific heat was determined using the Dulong–Petit law (C_p). Finally, the thermal conductivity (κ) was calculated from measured thermal diffusivity, specific heat and bulk density. These transport properties have been performed along two sets of directions, along P_{SPS} and are labelled with $\parallel$ or perpendicular to P_{SPS} with the label $\perp$.

3. Results and discussion

3.1. Structure refinement of In₂Ge₂Te₆

Crystals with suitable shapes and sizes were manually selected using a Zeiss V20 stereomicroscope. Large Ω scans performed on the crystals confirmed their good quality, as well as their estimated cell parameters. A selected single crystal of $In_2Ge_2Te_6$ was used for a full X-ray crystallographic analysis at room temperature; its dimensions are reported in Table 1. From a structure solution in the $P1$ space group, the electron density can be interpreted in terms of symmetry elements. This symmetry analysis led to a list of all the symmetry operations compatible with the lattice. On the basis of the agreement factor assigned to each symmetry operation, the space-group was found to be $R\bar{3}$. Plots of reciprocal lattice planes using Crysalis[38] (Fig. 1) were assembled from the different scans; they provide an overall view of the reciprocal space. These frames confirm the space-group with the existence condition: $-h + k + l = 3n$.

The structure of this compound has then been determined with Superflip[28] and the corresponding model was introduced in the program Jana2006.[29] All the atomic positions and anisotropic displacement parameters (ADPs) were refined for all the atoms (Table 2). Unit-cell parameter refinement from the single crystal X-ray diffraction data rapidly converged to $a = 7.0863(3)$ Å and $c = 21.206(2)$ Å with the rhombohedral space group $R\bar{3}$:H, a final agreement factor wR(all) of 0.0281 and a goodness of fit of 1.22. Details of the data collection and structure refinements are given in Table 1, while Table 3 lists interatomic distances.

3.2. Structural description of In₂Ge₂Te₆

In the $In_2Ge_2Te_6$ structure (Fig. 2), three crystallographic positions are fully occupied, one indium atom and one germanium atom are found at distinct 6c positions and the tellurium atom is situated at the 18f position. The structure is isostructural with the chromium chalcogenides $Cr_2Ge_2Te_6$,[16] and $Cr_2Si_2Te_6$.[14,15] This layered structure (Fig. 2a, ab plane) is constructed from an ABAB hexagonal close packing of tellurium atoms stacked

Table 1 Crystallographic data for single-crystal In₂Ge₂Te₆

Physical, crystallographic, and analytical data	
Formula	$In_2Ge_2Te_6$
Mol. wt (g mol^{-1})	1140.4
Cryst. syst.	Trigonal
Space group	$R\bar{3}$ (no. 148)
Cell parameters	
a, b(Å)	7.0863(3)
c (Å)	21.206(2)
V (Å^3)	922.20(11)
$Z = 3$	
Calculated density (g cm^{-3})	6.1604
Temperature (K)	293
Diffractometer	KappaCCD Nonius
Radiation	Mo Kα (0.71073 Å)
Crystal color	Black
Crystal description	Stick
Crystal size (mm^3)	$0.206 \times 0.022 \times 0.012$
Linear absorption coefficient (cm^{-1})	244.4
Scan mode	Ω/φ
Recording range 2θ (deg.)	$6.92 < 2\theta < 70.26$
hkl range	$-11 \leq h \leq 6$;
	$-11 \leq k \leq 11$; $-25 \leq l \leq 34$
No. of measured reflections	3114
Data reduction	
No. of independent reflections	904
R_{int} (%)	3.40
Absorption correction	Numerical method (SADABS)
Transmission coeff.	0.5220–0.7469
Independent reflections with $I > 3.0\sigma(I)$	621
Refinement	
R (%) (all/obs)	5.44/2.81
wR (%) (all/obs)	2.79/2.52
GOF (all/obs)	1.11/1.22
No. of refined parameters	17
Difference Fourier residues (e$^-$ Å^{-3})	$[-1.74, +4.79]$

along c. Ge atoms form dimers and are separated by $d_{(Ge–Ge)} = 2.4023(14)$ Å close to the sum of covalent radii of two Ge atoms (2.44 Å).[39] An equivalent bond length is found in $Cr_2Ge_2Te_6$ (2.426 Å). A residual electronic density peak of 4.79 e$^-$ Å^{-3} is found at the origin, meaning the center of the Ge pair. A regular octahedral coordination is found around In and Ge pairs. Interatomic distances found for indium are d(In–Te) = 2.9894(6) Å and d(In–Te) = 2.9855(6) Å, these distances are a bit larger than the sum of the In/Te ionic radii (0.81 + 2.11 = 2.92 Å), while interatomic distances found for Ge are d(Ge–Te) = 2.5630(5) Å indicating that Ge atoms are covalently bonded to Te atoms (1.22 + 1.36 = 2.58 Å). In one out of two consecutive slabs, germanium pairs and indium occupy the octahedral sites in a 1 : 2 ratio. Fig. 2b, representing the ac plane, shows that from one layer to another, the cationic arrangement is such that germanium pairs are translated by one third of the unit cell, following a rhombohedral symmetry. It has to be pointed out
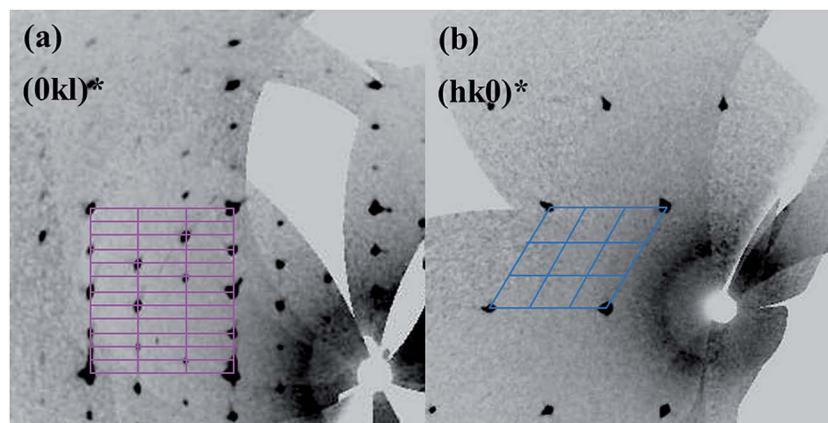
Fig. 1 Reconstruction with the Crysalis software of the $(0kl)^*$-(a) and $(hk0)^*$-(b) planes for single-crystal diffraction; cell edges are represented on each orientation.

Table 2 Refined coordinates, atomic displacement parameters (ADPs), and their estimated standard deviations for single-crystal $In_2Ge_2Te_6$

Atom	Wyckoff position	Occ.	x	y	z	U_{iso} ($\mathring{A}^2$)
In	6c	1	1/3	2/3	0.00034(3)	0.02018(17)
Ge	6c	1	0	0	0.05664(5)	0.0139(2)
Te	18f	1	0.65254(4)	0.00157(4)	0.08927(1)	0.01437(11)

Atom	U_{11}	U_{22}	U_{33}	U_{12}	U_{13}	U_{23}
In	0.01554(17)	0.01554(17)	0.0295(4)	0.00777(9)	0	0
Ge	0.0107(2)	0.0107(2)	0.0204(5)	0.00534(11)	0	0
Te	0.01209(14)	0.01509(14)	0.01694(16)	0.00754(11)	0.00122(11)	0.00012(11)

that $In_2Ge_2Te_6$ is not equivalent to its silicide derivative $InSiTe_3$ which crystallizes in the $AlSiTe_3$ structure type (space group $P\bar{3}$), where the silicon pairs are stacked on top of each other along the c direction.[20] In our case, the crystal is perfectly set in a rhombohedral space group, contrary to the lowering to the $P312$ space-group discussed by Carteaux *et al.* in $Cr_2Ge_2Te_6$.[16] Moreover, no residual electronic density can be found between the slabs, contrary to what was reported for $Mn_3Si_2Te_6$.[18] A van der Waals gap of 3.2824 Å separates each successive slab of unoccupied octahedra. In this gap, the tellurium interatomic distance $d(Te–Te) = 3.9881(5)$ Å is slightly smaller than the sum of the tellurium van der Waals radii 4.14 Å.[39]

Bond valence calculations have been performed after the structural refinement, the oxidation states In^{3+}, Ge^{3+} and Te^{2-} are confirmed and are in agreement with the oxidation states found, respectively, for Cr, Ge and Te in $Cr_2Ge_2Te_6$ from structural data and magnetic measurements.[16]

Table 3 Interatomic distances and their standard deviation in $In_2Ge_2Te_6$ given by the single-crystal study

At 1	At 2	Distance (Å)	At 1	At 2	Distance (Å)
In	In	4.0913(5)	Ge	Ge	2.4023(14)
In	In	4.0913(2)	Ge	Te	2.5630(5)
In	Te	2.9894(6)	Te	Te	3.9881(5)
In	Te	2.9855(6)	VdW gap		3.2824

3.3. Thermal stability and purity of the samples

The $InSiTe_3$, $Cr_2Si_2Te_6$, $Cr_2Ge_2Te_6$ and $In_2Ge_2Te_6$ sample purities were studied by means of X-ray powder diffraction. In all our attempts to synthesize $InSiTe_3$ and $Cr_2Si_2Te_6$, binary impurities were always observed in the samples even at a small scale, and this arguably comes from the incongruent melting of the $AMCh_3$ phases. In the case of $InSiTe_3$, an X-ray powder diffraction study *vs.* temperature demonstrates that incongruent melting happens between 473 K and 573 K, and the intensities of the impurity reflection gradually increase above (SVid. 1†). In the case of $Cr_2Si_2Te_6$, after increasing the temperature to 573 K while measuring thermoelectric properties, the bar shaped sample became darker and slightly bent. Consequently, a subsequent X-ray diffraction analysis performed on the bar shows an increase of the impurity reflection intensity. Thus, in order to avoid contributions of incongruent impurity formation, the thermoelectric studies of $InSiTe_3$ and $Cr_2Si_2Te_6$ were limited to up to 473 K.

A Rietveld refinement has been performed on the X-ray diffraction diagram of $Cr_2Ge_2Te_6$, resulting in $R_B = 6.06\%$ and $\chi^2 = 2.43$, and the purity of the sample is evidenced. SFig. 1† presents the Rietveld refinement plot of $Cr_2Ge_2Te_6$ and STable 2† gathers all information from Rietveld refinement. While EDX did not conclude the presence of any impurity, Rietveld refinement trials have also been done on $In_2Ge_2Te_6$; however no
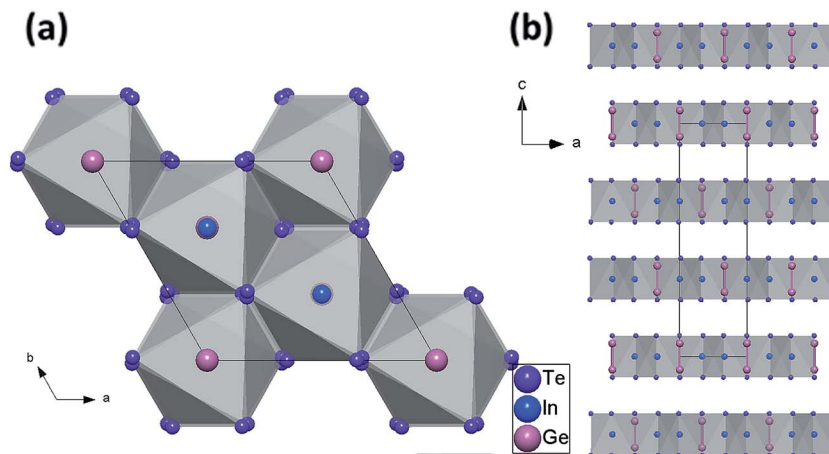
This journal is © The Royal Society of Chemistry 2017

J. Mater. Chem. A, 2017, **5**, 19406–19415 | **19409**

Fig. 2 Refined crystal structure from single-crystal analysis of $In_2Ge_2Te_6$ along [001]-(a) and [010]-(b); cell edges are represented by black lines. The stacking sequence one layer to another corresponds to a perfect crystal superposition of layers.

satisfactory reliability factors were obtained and some reflections could not be indexed given the cell parameters of the compound. Since no impurity matched those reflections, we consider these reflections to be intrinsic to the phase, and could result from stacking faults as already observed for this structural family.[16] To protect our instruments and avoid melting of the samples, we limited the range of measurements from room temperature to 673 K and 773 K, for $In_2Ge_2Te_6$ and $Cr_2Ge_2Te_6$, respectively. These maximum temperatures were set up to be approximately 50 K lower than the sintering temperature.

3.4. Thermoelectric properties of the $AMTe_3$ compounds

Recently, thermoelectric properties have been reported for $Cr_2Ge_2Te_6$ and a Cr-deficient sample.[24] The authors report ZT values of 0.35 and 0.45 at 823 K in the P_{SPS} direction, respectively, and a slight texture is noticeable. Here, the thermoelectric properties of four compounds of the $AMCh_3$ family are studied and compared to ref. 24.

Among the four samples, $Cr_2Ge_2Te_6$ exhibits the largest in-plane power factor ($PF_\perp = S_\perp^2/\rho_\perp$) with values ranging from 0.04 mW m^{-1} K^{-2} at 300 K to 0.64 mW m^{-1} K^{-2} at 600 K and remains constant up to 773 K (Fig. 3). Yang et al.[24] observed a constant increase of $PF_\perp$ for $Cr_2Ge_2Te_6$, with comparable values at RT and 773 K. Implying that at 600 K, our power factor is larger than theirs. At room temperature, $In_2Ge_2Te_6$ exhibits a $PF_\perp$ two orders of magnitude lower than that of $Cr_2Ge_2Te_6$. However, with increasing temperature, $PF_\perp$ reaches 0.09 W mm^{-1} K^{-2} at 673 K, only roughly 8 times less than for $Cr_2Ge_2Te_6$. The silicon homologues, $InSiTe_3$ and $Cr_2Si_2Te_6$, exhibit the lowest power factors with respective maxima of 1.04×10^{-3} and 3.52×10^{-3} W mm^{-1} K^{-2} at 473 K. The $\kappa_\parallel$ values of the four samples (Fig. 4) show that those of Cr-based samples are above unity in a wide temperature range, with values of 1.4 W m^{-1} K^{-1} and 1.15 W m^{-1} K^{-1} at room temperature for $Cr_2Ge_2Te_6$ and $Cr_2Si_2Te_6$. The $Cr_2Si_2Te_6$ thermal conductivity decreases below 1 W m^{-1} K^{-1} at 473 K, while for $Cr_2Ge_2Te_6$ temperatures as large as 650 K are necessary
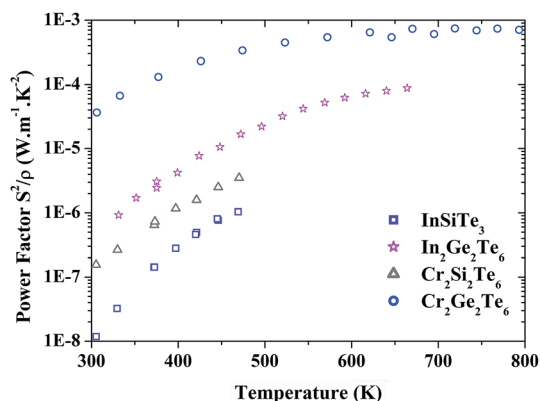
Fig. 3 Temperature dependence of the power-factor for $InSiTe_3$, $In_2Ge_2Te_6$, $Cr_2Si_2Te_6$ and $Cr_2Ge_2Te_6$ from 300 to 800 K depending on the compound. These values correspond to the measurements in the in-plane direction.
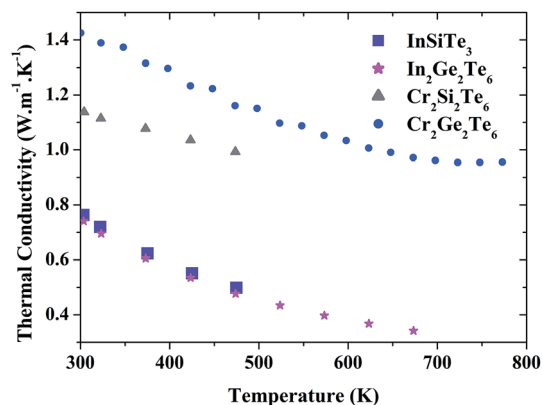

Fig. 4 Temperature dependence of the thermal conductivity for $InSiTe_3$, $In_2Ge_2Te_6$, $Cr_2Si_2Te_6$ and $Cr_2Ge_2Te_6$ from 300 to 800 K depending on the compound. These values correspond to the measurements in the out-of-plane direction.

19410 | *J. Mater. Chem. A*, 2017, **5**, 19406–19415

This journal is © The Royal Society of Chemistry 2017

to reach unity. For indium-based samples $\kappa_\parallel$ follow the same tendency in their respective range of thermal stability, going from 0.75 W m^{-1} K^{-1} at room temperature for both samples to 0.34 W m^{-1} K^{-1} at 673 K for In$_2$Ge$_2$Te$_6$, and 0.49 W m^{-1} K^{-1} at 473 K for InSiTe$_3$. From these data, and being limited with the peculiar restricted thermal stability of InSiTe$_3$ and Cr$_2$Si$_2$Te$_6$, we decided to further study the other two compositions, the potentially best candidates for the largest thermoelectric values, *i.e.* In$_2$Ge$_2$Te$_6$ and Cr$_2$Ge$_2$Te$_6$.

3.5.   Anisotropy of Cr$_2$Ge$_2$Te$_6$, thermoelectric properties and texture analysis

Layered structures often develop crystallographic orientations (texture) when subjected to uniaxial solicitations as in spark plasma sintering.[40] This texture can result in anisotropic macroscopic physical properties if the single crystal property tensors are intrinsically anisotropic themselves. This might be the case for our samples for Seebeck, electrical resistivity and thermal conductivity tensors. We do not intend here to optimize anisotropic and macroscopic properties, but since Cr$_2$Ge$_2$Te$_6$ properties measured along P_{SPS} ($\rho_\parallel$, $\kappa_\parallel$, $S_\parallel$) and perpendicular to it ($\rho_\perp$, $\kappa_\perp$, $S_\perp$) showed different magnitudes we decided to evaluate if texture could be the explanation for them (Fig. 5).

The electrical resistivities show a typical semi-conductor behavior with a decrease of the resistivity with temperature from room temperature to 773 K (Fig. 5a). In this temperature range, we observe a roughly 60% larger $\rho_\parallel$ contribution compared to $\rho_\perp$, observing that $\rho_\perp$ goes from 1.77 Ω cm to typically a hundredth of this value at 773 K, *i.e.* 0.0133 Ω cm, similarly to the Yang *et al.*[24] observation. Cr$_2$Ge$_2$Te$_6$ is a p-type semi-conductor with relatively large values of Seebeck coefficients (Fig. 5b). The Seebeck coefficient decreases with temperature, from about $S_\parallel = 800$ µV K^{-1} at room temperature to 315 µV K^{-1} at 773 K. Interestingly, $S_\perp$ and $S_\parallel$ evolve quite linearly with temperature with a slightly different slope. This results in an increasing anisotropy towards lower temperatures, an observation consistent with that of Yang *et al.* who reported a pronounced Seebeck anisotropy at room temperature.[24] $S_\perp$ is larger by almost 120 µV K^{-1} compared to $S_\parallel$ at 300 K, *i.e.* a bit less than 20% anisotropy, but this anisotropy practically vanishes at 773 K. Thermal conductivities show a much larger anisotropy (Fig. 5c) with $\kappa_\perp$ 30% larger than $\kappa_\parallel$ over the whole range of temperatures. $\kappa_\perp$ is about 1.8 W m^{-1} K^{-1} at 300 K, and decreases to 1.3 W m^{-1} K^{-1} at 773 K. The calculated electronic thermal conductivity component is negligible up to 600 K, and then above it, a separation of the lattice component (dotted line, Fig. 5c) from the total thermal conductivity can be witnessed. At 773 K, the electronic contribution is about 10% of the total
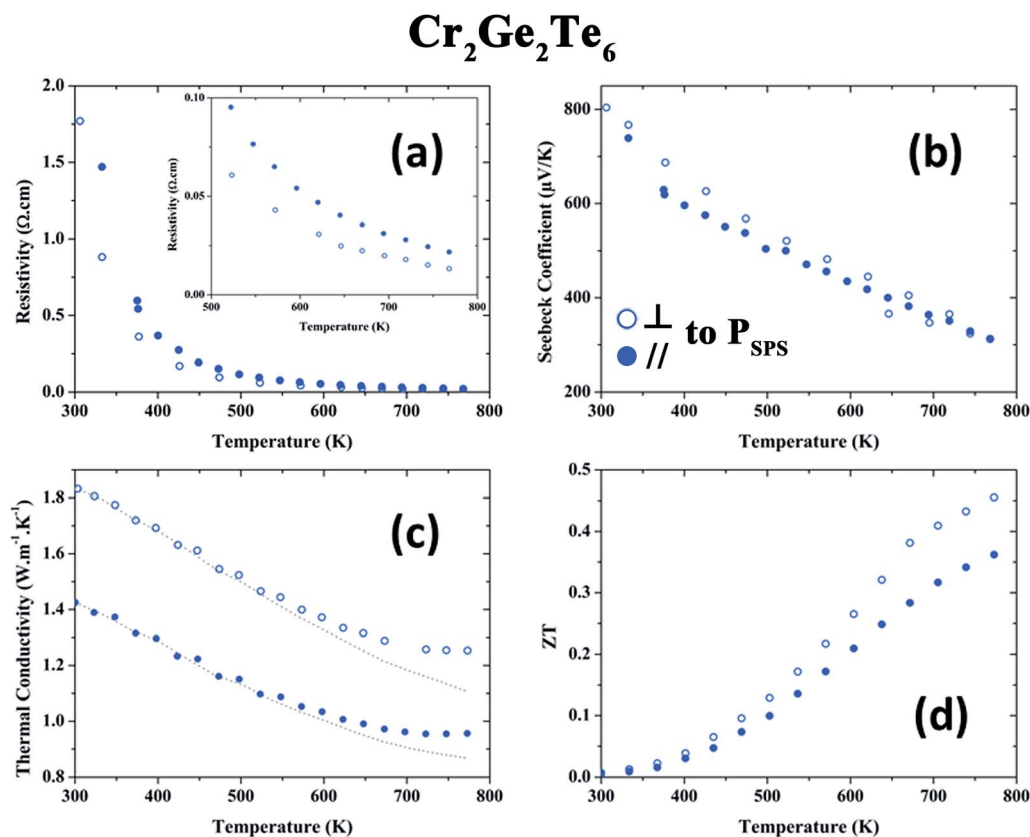

Fig. 5 Temperature dependence of the (a) resistivity with a zoom in temperature in the inset, (b) Seebeck coefficient, (c) thermal conductivity, and (d) the resulting *ZT* for the phase Cr$_2$Ge$_2$Te$_6$, from room temperature to 773 K. Empty circles: $\perp$ and filled circles: $\parallel$ values. The dotted line in (c) shows the calculated lattice thermal conductivity.

$\kappa_\perp$ and $\kappa_\parallel$ components. We calculated ZT from the three previous values, obtaining an increasing ZT from 300 K to 773 K, achieving 0.45 and 0.37 at 773 K for $ZT_\perp$ and $ZT_\parallel$, respectively. These values are slightly above those found by Yang *et al.*,[24] with ZTs at 773 K of 0.34 and 0.3 for $\perp$ and $\parallel$ directions.

In order to ascertain if such anisotropies could come from texture, a quantitative texture analysis was performed. After full combined analysis refinement, obtained with a goodness of fit of 1.2, we obtained cell parameters of $a = 6.81654(9)$ Å and $c = 20.5322(3)$ Å, coherent with the literature. Atomic occupations and thermal displacement parameter refinement showed that within our experimental conditions these two parameters were not approached with enough reliability and were consequently fixed to $B_{iso} = 0.2$ and all occupation factors to 1. Atomic positions were successfully refined to: $x_{Te} = 0.6681(1)$, $y_{Te} = -0.02867(6)$, $z_{Te} = 0.25024(4)$, $z_{Cr} = 0.3300(1)$ and $z_{Ge} = 0.06178(4)$. Such positions fully agree with previously published structural determinations. The refined mean crystallite sizes are 140(1) nm along the c-axis and 32(1) nm perpendicularly. The OD ranged from 0 m.r.d. to 4.73 m.r.d. (with a texture index of 1.3 m.r.d.[2]) and showed only one fiber component with P_{SPS} as the fiber axis. Such texture strength is rather smooth and usual for non-optimized SPS synthesized samples. The corresponding recalculated pole figures (Fig. 6) show that the mean c axis is aligned $\parallel$ to P_{SPS}, on a Gaussian distribution of approximately $80°$ FWHM.

The geometric mean approach allows us to estimate, for a given single crystal tensor and the measured OD of a material, the corresponding macroscopic tensor. Since there are no data available for $Cr_2Ge_2Te_6$ single crystals in the literature, such a procedure only allows an estimate of single crystal anisotropy when the OD is known as in our case. We tried to reproduce the typical $\kappa_\perp = 1.8$ W m^{-1} K^{-1} and $\kappa_\parallel = 1.4$ W m^{-1} K^{-1} values at 300 K, and obtained with our refined OD, $\kappa_{11} = \kappa_{22} = 8$ W m^{-1} K^{-1} and $\kappa_{33} = 0.08$ W m^{-1} K^{-1} for the single crystal values. Such a large anisotropy ratio of 100 looks large but not impossible, specifically in strongly layered systems. For instance, a 10 000 ratio could be observed in Bi2212 high T_c superconductor single crystal electrical resistivities.[41,42] However we do not have such an example for thermal conductivity; an anisotropic ratio of 100 still remains relatively exceptional, and we conclude that the low texture strength cannot explain alone the thermal conductivity anisotropy observed in our samples. The observed resistivity and Seebeck coefficient anisotropies are less pronounced and could be the result of a smooth texture.
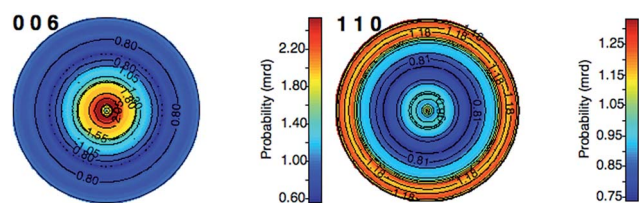

Fig. 6 {006} and {110} pole figures for the $Cr_2Ge_2Te_6$ sample. Equal area projections. The P_{SPS} axis is the center of the pole figures.

3.6. Thermoelectric properties of $In_2Ge_2Te_6$, low thermal conductivity and transmission electron microscopy study

Similar to $Cr_2Ge_2Te_6$, we decided to perform thermoelectric measurements in two directions (Fig. 7). As opposed to $Cr_2Ge_2Te_6$, no significant anisotropy of the properties can be observed except a thermal conductivity one of about 10% over the whole temperature range, smaller than the one observed in $Cr_2Ge_2Te_6$. A p-type semi-conductor behavior is also exhibited. With a 460 Ω cm resistivity at room temperature (Fig. 7a), $In_2Ge_2Te_6$ is about two orders of magnitude more resistive than $Cr_2Ge_2Te_6$. However, at 673 K, only one order of magnitude differs between the two compounds, with $In_2Ge_2Te_6$, $\rho_{673\ K} = 0.03$ Ω cm. The Seebeck coefficient (Fig. 7b) decreases quasi-linearly from 1120 μV K^{-1} at room temperature to 520 μV K^{-1} at 673 K. These values are about 300 to 200 μV K^{-1} larger than that of its Cr-derivative. κ ranges from 0.78 W m^{-1} K^{-1} at room temperature to 0.35 W m^{-1} K^{-1} at 673 K. The electronic contribution is negligible over the temperature range. Taking into account that no anisotropy is observed neither on the resistivity, nor the Seebeck coefficient or resulting ZT, no quantitative texture analysis appears necessary for this sample. The ZT (Fig. 7d) increases regularly over the temperature range reaching a maximum of 0.18 at 673 K.

As discussed in Section 3.3, Rietveld refinement did not permit us to get satisfactory reliability factors, a TEM study has then been undertaken for this sample. EDS analysis performed on several crystallites validates the purity of the sample. Thus, additional reflections observed on the X-ray diffraction plot are confirmed to be intrinsic to the material. Lowering of the symmetry due to stacking faults between the layers has already been observed in $Cr_2Ge_2Te_6$, as suggested in ref. 16, breaking the rhombohedral setting at short range distances. The results of the microscopy analysis are gathered in Fig. 8a–c for the [010] or [100] zone axis, and Fig. 8d for the [001] zone axis. The HAADF image (Fig. 8d) and corresponding electron diffraction pattern allow indexing in the $R\bar{3}$:H space group with the cell parameters of $In_2Ge_2Te_6$. In Fig. 8d (both upper and lower), no particular disorder is visible. In Fig. 8c, a portion of an HAADF image with a perfect stacking is presented. A perfect stacking between the slabs should follow the straight yellow line. Each germanium pair column should stack with an offset of one third of the unit cell. In addition, a ratio of 2 : 1 for indium and germanium pairs, respectively, is followed along the a axis. As shown along [010] (Fig. 8a), the ratio is maintained, but perfect stacking almost never occurs, meaning that there is a high density of stacking faults in the material. The sequence of faults is erratic, and produces diffuse lines in the electron diffraction pattern in Fig. 8a for reflections with $h \neq 3n$ (or $k \neq 3n$ in the [100] direction). If on some slabs the crystalline structure in a rhombohedral obverse orientation is rotated by $180°$ around c, then on the same (010) plane, it will produce reflections following the condition $h - k + l = 3n$ (R reverse orientation) and the original condition $-h + k + l = 3n$ (R obverse orientation). This phenomenon can be understood as nano-twin, in a local range. Since the disorder is random, these reflections are not punctual but diffuse, and are represented by diffuse lines over

19412 | *J. Mater. Chem. A*, 2017, **5**, 19406–19415

This journal is © The Royal Society of Chemistry 2017
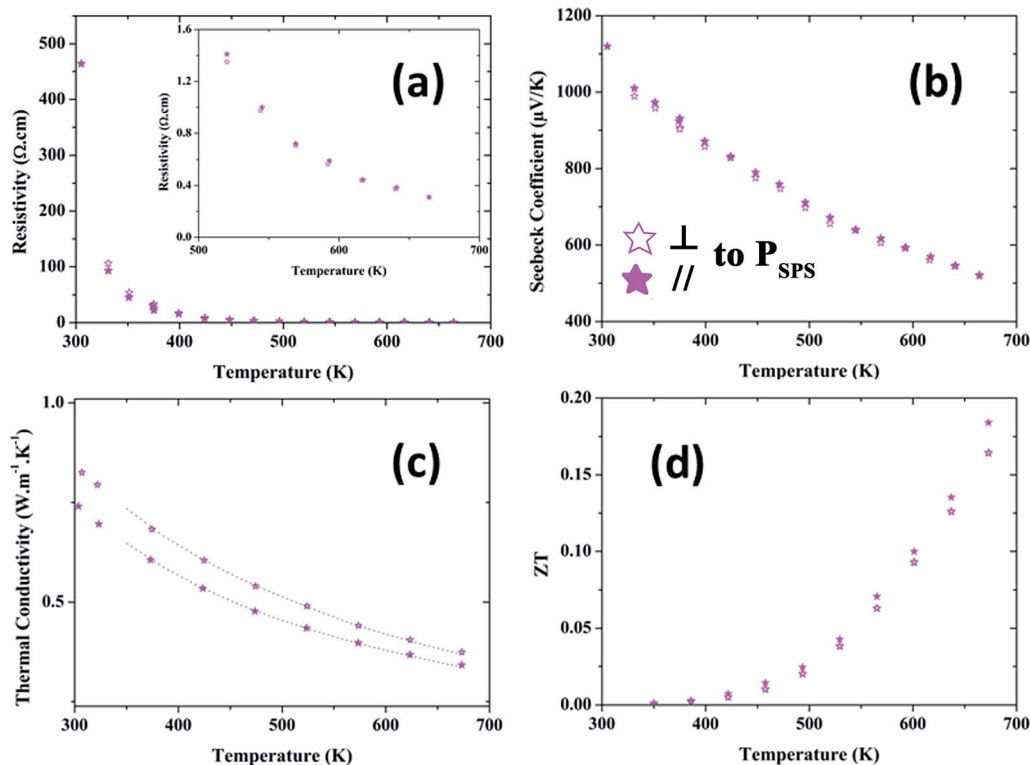
Fig. 7 Temperature dependence of the (a) resistivity with a zoom in temperature in the inset, (b) Seebeck coefficient, (c) thermal conductivity, and (d) the resulting ZT for the phase $In_2Ge_2Te_6$, from room temperature to 673 K. Empty circles: $\perp$ and filled circles: $\parallel$ values. The dotted line in (c) shows the calculated lattice thermal conductivity.

the reflections given by $h \neq 3n$. Moreover, bright reflections with $h = 3n$ and $l = 3n$ will be strengthened considering that stacking one germanium pair above another is identical to

Fig. 8 (a) Experimental [010] oriented HAADF-image of $In_2Ge_2Te_6$ with the presence of stacking faults along c and the associated effect on the diffraction pattern. (b) A dislocation is observed in this image. (c) Perfect stacking sequence corresponding to the single-crystal case. (d) Experimental [001] oriented image associated with the electron diffraction showing no or random disorder along this direction.

observe, in a short range, the $AlSiTe_3$ structure type (where the c parameter of $In_2Ge_2Te_6$ corresponds to the $3c'$ parameter of the $AlSiTe_3$ structure type).

Fig. 9a presents the Le Bail fit performed on the X-ray diffraction diagram of $In_2Ge_2Te_6$, with the space group $R\bar{3}$ and cell parameters $a = 7.10998(1)$ Å and $c = 21.2629(8)$ Å. Most of the reflections fit with the Le Bail plot; however as observed in the zoomed section of this diagram (Fig. 9(d-left bubble)), the $3c'$ stacking model ($Cr_2Ge_2Te_6$ stacking type Fig. 9(c-lower)) does not fit with satellite reflections. As seen in Fig. 8, the perfect stacking sequence is not followed and a larger unit cell could be used to fit short range disorder. Fig. 9b shows the Le Bail fit plot when different stacking unit cells are considered. To fit all satellite reflections three different stacking models had to be added, all in the $P\bar{3}$ space group to break the rhombohedral symmetry. With the added $4c'$, $5c'$ and $7c'$ stacking sequences (with examples shown in Fig. 9e), we observe that the model is now fitting with the satellite reflections. Eventually, this model could be applied successfully to all phases in this family of compounds. In the single-crystal study, stacking faults could be an explanation why some residual electronic density is observed in the center of the Ge pairs.

This disorder along the c axis, as well as dislocations (Fig. 8b), surely lowers the phonon mean free path along this direction of the crystals. Consequently, even with the weak textures observed under SPS conditions in such phases, the
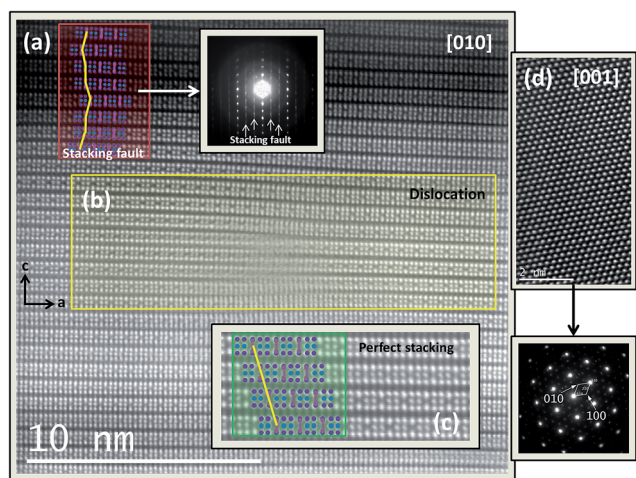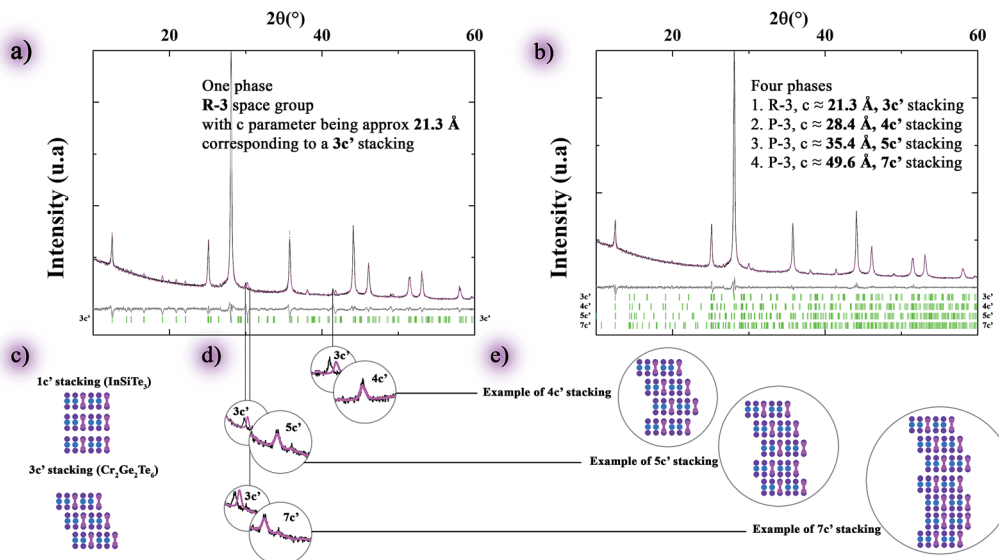
Fig. 9 (a) Le Bail fit of the X-ray diffraction pattern of $In_2Ge_2Te_6$ with the 3c' stacking sequence (as clearly shown in the picture text). (b) Le Bail fit of the X-ray diffraction pattern of $In_2Ge_2Te_6$ with four stacking sequence unit cells, 3c', 4c', 5c', and 7c' (as clearly shown in the picture text). Black line, purple line, grey line, and green bars correspond to observed, calculated, (Obs-Calc) intensities and Bragg position of the unit cells, respectively. (c) Perfect stacking sequence corresponding to the single-crystal case of $InSiTe_3$ (upper) and $Cr_2Ge_2Te_6$ (lower). (d) Left bubbles: zoom of the Le Bail fit in the 3c' case, right bubbles: zoom of the Le Bail fit with the four stacking sequence unit cells. (e) Some examples of different possible sequences in the 4c', 5c', and 7c' stacking sequence unit cells.

disorder contributes to the lowering of $\kappa_{\parallel}$ while $\kappa_{\perp}$ is less affected. The same reasoning can be applied to any phase of this family. In the case of $Cr_2Ge_2Te_6$ and $Cr_2Si_2Te_6$, the question is raised as to why we obtain a larger lattice thermal conductivity than in the case of $In_2Ge_2Te_6$ and $InSiTe_3$. First of all, indium is twice heavier than chromium atoms, which results in increased phonon scattering. Secondly, other effects like grain sizes and impurities at the grain boundaries could lower the mean free path in $In_2Ge_2Te_6$ more than in the other samples. Finally, regarding bond distances between $Cr_2Ge_2Te_6$ and $In_2Ge_2Te_6$, d_{In-Te} is 0.2 Å larger than d_{Cr-Te}, and will affect phonon frequencies, resulting in a different scattering process.

4. Conclusions

A new ternary indium-chalcogenide with germanium pairs $In_2Ge_2Te_6$ was synthesized by a solid-state reaction. Its crystal structure has been determined; it crystallizes in the $R\bar{3}$:H space-group and the following cell parameters were refined: $a = 7.0863(3)$ Å and $c = 21.206(2)$ Å. It belongs to the $MnPSe_3$ structure type family. We successfully synthesized bulk samples and studied the thermoelectric properties of four compounds of this $AMCh_3$ family. While $InSiTe_3$ and $Cr_2Si_2Te_6$ were found to be very resistive, $Cr_2Ge_2Te_6$ and $In_2Ge_2Te_6$ show both p-type semi-conductor behaviors with large Seebeck coefficients of more than 300 µV K^{-1}. Thermal conductivities were found to be around 1 W m^{-1} K^{-1} for $Cr_2Ge_2Te_6$ at 773 K and 0.35 W m^{-1} K^{-1} for $In_2Ge_2Te_6$ at 673 K. $InSiTe_3$ and $Cr_2Si_2Te_6$ still present low thermal conductivities, especially $InSiTe_3$ with values below unity. This could be explained by a massive amount of stacking faults between the layers as revealed by TEM, resulting in

symmetry breaking at the local scale. The thermal properties of $Cr_2Ge_2Te_6$ exhibit 30% anisotropy, partly explained by the crystallite orientations that reach a maximum orientation density of only 4.73 m.r.d. along the pressing direction. Final ZT was calculated at 0.45 (773 K) and 0.18 (673 K) for $Cr_2Ge_2Te_6$ and $In_2Ge_2Te_6$.

Conflicts of interest

There are no conflicts of interest to declare.

Acknowledgements

References

1 M.-H. Fang, H.-D. Wang, C.-H. Dong, Z.-J. Li, C.-M. Feng, J. Chen and H. Q. Yuan, *EPL*, 2011, **94**, 27009.
2 C. Wan, Y. Wang, N. Wang and K. Koumoto, *Materials*, 2010, **3**, 2606–2617.
3 R. Nunna, F. Gascoin and E. Guilmeau, *J. Alloys Compd.*, 2015, **634**, 32–36.
4 F. Gascoin, N. Raghavendra, E. Guilmeau and Y. Bréard, *J. Alloys Compd.*, 2012, **521**, 121–125.
5 X. Lu, D. T. Morelli, Y. Xia, F. Zhou, V. Ozolins, H. Chi, X. Zhou and C. Uher, *Adv. Energy Mater.*, 2013, **3**, 342–348.

19414 | *J. Mater. Chem. A*, 2017, **5**, 19406–19415

This journal is © The Royal Society of Chemistry 2017

6 T. Barbier, S. Rollin-Martinet, P. Lemoine, F. Gascoin, A. Kaltzoglou, P. Vaqueiro, A. V. Powell and E. Guilmeau, *J. Am. Ceram. Soc.*, 2016, **99**, 51–56.

7 F. Gascoin and A. Maignan, *Chem. Mater.*, 2011, **23**, 2510–2513.

8 R. Lefèvre, D. Berthebaud, O. Perez, D. Pelloquin, S. Hébert and F. Gascoin, *Chem. Mater.*, 2015, **27**, 7110–7118.

9 R. Lefèvre, D. Berthebaud, S. Bux, S. Hébert and F. Gascoin, *Dalton Trans.*, 2016, **45**, 12119–12126.

10 D. Berthebaud, K. R. S. Preethi Meher, D. Pelloquin and A. Maignan, *J. Solid State Chem.*, 2014, **211**, 184–190.

11 D. Berthebaud, O. Perez, J. Tobola, D. Pelloquin and A. Maignan, *J. Solid State Chem.*, 2015, **230**, 293–300.

12 R. Lefèvre, D. Berthebaud, O. Pérez, D. Pelloquin, S. Boudin and F. Gascoin, *J. Solid State Chem.*, 2017, **250**, 114–120.

13 E. Sandre, V. Carteaux and G. Ouvrard, *C. R. Acad. Sci., Ser. II: Mec., Phys., Chim., Sci. Terre Univers*, 1992, **314**, 1151–1156.

14 G. Ouvrard, E. Sandre and R. Brec, *J. Solid State Chem.*, 1988, **73**, 27–32.

15 R. E. Marsh, *J. Solid State Chem.*, 1988, **77**, 190–191.

16 V. Carteaux, D. Brunet, G. Ouvrard and G. Andre, *J. Phys.: Condens. Matter*, 1995, **7**, 69.

17 J. Gopalakrishnan and K. S. Nanjundaswamy, *Mater. Res. Bull.*, 1988, **23**, 107–112.

18 H. Vincent, D. Leroux, D. Bijaoui, R. Rimet and C. Schlenker, *J. Solid State Chem.*, 1986, **63**, 349–352.

19 R. Rimet, C. Schlenker and H. Vincent, *J. Magn. Magn. Mater.*, 1981, **25**, 7–10.

20 E. Sandre, V. Carteaux, A. M. Marie and G. Ouvrard, *J. Alloys Compd.*, 1994, **204**, 145–149.

21 W. Klingen, R. Ott and H. Hahn, *Z. Anorg. Allg. Chem.*, 1973, **396**, 271–278.

22 W. Klingen, G. Eulenberger and H. Hahn, *Z. Anorg. Allg. Chem.*, 1973, **401**, 97–112.

23 B. Siberchicot, S. Jobic, V. Carteaux, P. Gressier and G. Ouvrard, *J. Phys. Chem.*, 1996, **100**, 5863–5867.

24 D. Yang, W. Yao, Q. Chen, K. Peng, P. Jiang, X. Lu, C. Uher, T. Yang, G. Wang and X. Zhou, *Chem. Mater.*, 2016, **28**, 1611–1615.

25 *SAINT*, Brucker AXS Inc., Madison, Wisconsin, USA, 2004.

26 *APEX2*, Brucker AXS Inc., Madison, Wisconsin, USA, 2004.

27 G. M. Sheldrick, *SADABS, Program for Empirical Absorption Correction of Area Detector Data*, University of Göttingen, Germany, 1996.

28 L. Palatinus and G. Chapuis, *J. Appl. Crystallogr.*, 2007, **40**, 786–790.

29 V. Petricek, M. Dusek and L. Palatinus, *Z. Kristallogr. Cryst. Mater.*, 2014, **229**, 345–352.

30 J. Rodríguez-Carvajal and T. Roisnel, *Comm. Powder Diffr. Int. Union Crystallogr.*, 1998.

31 T. Roisnel and J. Rodríguez-Carvajal, R. Delhez and E. J. Mittenmeijer, *Materials Science Forum, Proceedings of the Seventh European Powder Diffraction Conference*, 2000, pp. 118–123.

32 D. Chateigner, *Combined Analysis*, Wiley-ISTE, 2010.

33 L. Lutterotti, S. Matthies and H. Wenk, *National Research Council of Canada*, ed. J. A. Spunar, Ottawa, 1999, pp. 1599–1604.

34 M. Morales, D. Chateigner, L. Lutterotti and J. Ricote, *Mater. Sci. Forum*, 2002, **408–412**, 113–118.

35 L. Lutterotti, D. Chateigner, S. Ferrari and J. Ricote, *Thin Solid Films*, 2004, **450**, 34–41.

36 D. Chateigner, *J. Appl. Crystallogr.*, 2005, **38**, 603–611.

37 N. C. Popa, *J. Appl. Crystallogr.*, 1998, **31**, 176–180.

38 *CrysAlisPRO*, Agilent Technologies UK Ltd, Yarnton, England, 2014.

39 R. D. Shannon, *Acta Crystallogr., Sect. A: Cryst. Phys., Diffr., Theor. Gen. Crystallogr.*, 1976, **32**, 751–767.

40 Q. Lognoné, F. Gascoin, O. I. Lebedev, L. Lutterotti, S. Gascoin and D. Chateigner, *J. Am. Ceram. Soc.*, 2014, **97**, 2038–2045.

41 T. Watanabe, T. Fujii and A. Matsuda, *Phys. Rev. Lett.*, 1997, **79**, 2113–2116.

42 A. Dellicour, B. Vertruyen, M. O. Rikel, L. Lutterotti, A. Pautrat, B. Ouladdiaf and D. Chateigner, *Materials*, 2017, **10**, 534.